

JGR Space Physics

RESEARCH ARTICLE

10.1029/2020JA028918

Key Points:

- GWs in the MLT at Andes have preferential propagation in the meridional direction, leading to stronger amplitudes in the meridional wind
- Vertical wind has much shallower saturated spectrum slope and far steeper spectral tail in both frequency and vertical wavenumber spectra
- Obvious difference between the vertical and horizontal wind spectra suggests that the vertical wind should obey the different spectral laws

Correspondence to:





K. M. Huang,
hkm@whu.edu.cn

Citation:

Huang, K. M., Liu, H., Liu, A. Z., Zhang, S. D., Huang, C. M., Gong, Y., & Ning, W. H. (2021). Investigation on spectral characteristics of gravity waves in the MLT using lidar observations at Andes. *Journal of Geophysical Research: Space Physics*, 126, e2020JA028918. <https://doi.org/10.1029/2020JA028918>

Received 8 NOV 2020
Accepted 25 FEB 2021

Investigation on Spectral Characteristics of Gravity Waves in the MLT Using Lidar Observations at Andes

Kai Ming Huang^{1,2,3} , Hang Liu^{1,2,3} , Alan Z. Liu⁴ , Shao Dong Zhang^{1,2} , Chun Ming Huang^{1,2} , Yun Gong^{1,2} , and Wu Han Ning^{1,2}

¹School of Electronic Information, Wuhan University, Wuhan, China, ²Key Laboratory of Geospace Environment and Geodesy, Ministry of Education, Wuhan, China, ³State Observatory for Atmospheric Remote Sensing, Wuhan, China, ⁴Department of Physical Science, Embry Riddle Aeronautical University, Daytona Beach, FL, USA

Abstract Based on observations from lidar at Andes, we study the features of gravity wave activities and their spectra in the mesosphere and lower thermosphere (MLT). Case analysis shows that a quasi-monochromatic inertia-gravity wave (IGW) dominates the perturbation fields, with clearly downward phase progression in the wind and temperature fields. Statistical investigation shows that the dominant waves in the MLT over Andes have the typical temporal and spatial scales of IGWs and show the preferential propagation in the meridional direction relative to in the zonal direction. The preferential propagation direction causes larger spectral peak and steeper spectral slope in the meridional wind as compared to the zonal counterpart. The 27-night observations indicate that the frequency (vertical wavenumber) spectrum has the slopes of about -1.4 (-1.5), -1.7 (-2.0), and -2.3 (-2.6) in the zonal wind, meridional wind, and relative temperature perturbations, more or less deviated from the universal spectral index of $-5/3$ (-3), respectively. The vertical wind has a steeper spectral tail in both the frequency and wavenumber spectra, which is different from the other three components. In the saturated spectrum region, the frequency and vertical wavenumber spectra have the slopes of -0.4 and -1.1 in the vertical wind, which are much shallower than those in the zonal and meridional winds, respectively. In the spectral tail region, the frequency and wavenumber spectrum slopes of -2.2 and -3.5 are far steeper relative to their saturated spectrum slopes. This suggests that the vertical wind should obey the different spectral laws from the horizontal winds.

1. Introduction

It is known for decades that gravity waves (GWs) have a substantial influence on the mean circulation and thermal structure of the middle and upper atmosphere because they transport energy and momentum from the lower atmosphere and deposit them into the middle and upper atmosphere due to the instability (Fritts & Alexander, 2003; Holton, 1982). As GWs generated in the lower atmosphere propagate upward, their amplitudes increase exponentially with altitude because of the decrease of atmospheric density. When the amplitude reaches the critical value, GWs break up as a result of convective or dynamic instability or critical level filtering and then release energy and momentum to the background flow, which is regarded as wave saturation and dissipation process (Hickey et al., 2003; Lindzen, 1981).

As a delicate method, hodograph technique is extensively utilized to extract the predominant inertia-gravity wave (IGW) from the observational profiles of radiosonde (Huang et al., 2018; Tsuda et al., 1994; Vincent & Alexander, 2000; Yamamori & Sato, 2006; S. D. Zhang & Yi, 2005; S. D. Zhang et al., 2012, 2017), radar (Gavrilov et al., 2000; Nicolls et al., 2010; Suzuki et al., 2013; M. Yamamoto et al., 1987; Zhou & Morton, 2006), and lidar (Cai et al., 2014; Chen et al., 2013, 2016; Collins et al., 1994; Hu et al., 2002; T. Li et al., 2007; Lu et al., 2015, 2017; Rajeev et al., 2003; Xu et al., 2006). Combined with Doppler shifting equation, this technique can estimate the temporal and spatial parameters of quasi-monochromatic IGW, such as wave period, wavelength, and propagation direction. A large number of observations indicate that GWs have typical horizontal wavelengths of tens to thousands of kilometers, vertical wavelengths of a few to tens of kilometers, and frequencies of minutes to days (Cai et al., 2014, 2017; Chen et al., 2013; Lu et al., 2015; Suzuki et al., 2013; Vincent & Alexander, 2000; Wang et al., 2005; Yamamori & Sato, 2006; Yoshiki et al., 2004; Yuan et al., 2016; S. D. Zhang & Yi, 2005, 2007; Zhou & Morton, 2006). In addition, broad spectral analysis method is widely used to investigate the structure of atmospheric GW power spectral density (PSD) and to

obtain total energy and momentum of GWs with a spectral range (Acott et al., 2011; Ern et al., 2004; H. Y. Li et al., 2016; Yuan et al., 2014, 2016; S. D. Zhang et al., 2012, 2013).

The universal spectrum was suggested by VanZandt (1982). The atmospheric horizontal wind, temperature, and density perturbations exhibit an almost invariant power law shape in the saturated spectra region regardless of altitude, season, and location, thus the almost invariant spectrum was called “universal” spectrum. The universal spectrum has the canonical slopes of $-5/3$ in the frequency spectrum and -3 in the vertical wavenumber spectrum on a logarithmic coordinate. Specific wave sources endow the generated wavefield with their own spectral features, thus source characteristics do not explain the formation of the universal spectrum. Wave propagation in the sheared wind and nonuniform temperature can make the wave spectrum fade away from the source features, and nonlinear interaction can shape the wave spectrum through energy exchange among different spectral components (Huang et al., 2009, 2012; Snively, 2017). In this case, the universal characteristic is generally attributed to the combined effect of superposition of waves excited by different sources, wave propagation, and extensive nonlinear interaction. Meanwhile, as wave momentum and energy eventually deposit to the background flow in the form of turbulent motion due to the instability, wave dissipation also plays an important role in shaping the PSD slope. Hereby, based on assumption of different dissipation mechanisms, some spectral theories, such as linear instability theory (Dewan & Good, 1986; Smith et al., 1987), diffusive damping theory (Weinstock, 1989), diffusive filtering theory (Gardner, 1994; Weinstock, 1989; Zhu, 1994), and Doppler-spread theory (Hines, 1991, 1997), were suggested to interpret the formation of the universal spectrum. All the theories can give the canonical PSD indices of the horizontal wind and temperature perturbations; however, these spectral theories also predict the different PSD index in the vertical wind perturbation based on the GW polarization relations among different perturbation components. Hence, the vertical wind spectrum observed by various measurements can provide insight into the dissipation mechanisms of GWs and the spectral theories.

In last few decades, many observational studies improved our understanding of the universal spectra. The characteristics of vertical wavenumber spectrum in the horizontal winds are widely investigated from the troposphere to the mesosphere and lower thermosphere (MLT) based on radiosonde (Guharay et al., 2010; Huang et al., 2018; S. D. Zhang et al., 2017), radar (Dutta et al., 2005; Larsen et al., 1986; Qing et al., 2014), and lidar (Gardner et al., 1998; Senft & Gardner, 1991; Yang et al., 2006) measurements. These observations indicated that the vertical wavenumber spectrum in the horizontal winds has a PSD slope range of about -1.5 to -3.2 in the different atmospheric layers. Radar and lidar can obtain the high time resolution horizontal winds, which raises the possibility of investigating the frequency spectrum in the horizontal wind perturbations. The frequency spectra in the zonal and meridional winds have the PSD slope between -1.5 and -2.2 in radar (Hoffmann et al., 2010; Larsen et al., 1986; Y. Yamamoto et al., 1996) and lidar (Senft & Gardner, 1991; Yang et al., 2006) data. A lot of observations showed that the index ranges of frequency and vertical wavenumber spectra in the temperature fluctuations are approximately the same as those in the horizontal wind perturbations (Chen et al., 2016; Cot, 2001; Guharay & Sekar, 2011; Guo et al., 2017; Huang et al., 2018; Wu et al., 2006; Yang et al., 2010). It can be noted that the observed frequency (vertical wavenumber) spectrum slope exhibits a change around the canonical value of $-5/3$ (-3) derived from the spectral theories. The variability is usually attributed to the unsaturated GWs, background conditions, and wave sources.

As for the vertical wind, not only these spectral theories deduce different spectral slopes but also the limited observations showed substantial difference in the PSD index. For instance, the vertical wavenumber in the vertical wind has a same spectral slope of -3 as in the horizontal winds and temperature in the linear instability spectrum theory (Dewan & Good, 1986; Smith et al., 1987), but a spectral slope near 1 in the diffusive filtering theory (Gardner, 1994). Based on the vertical wind in the MLT measured by lidar, the slope of the frequency (vertical wavenumber) spectrum is driven to be near 0 (-1.4) over Maui (Gardner et al., 1995), and in the range of -0.59 to -1.2 (-0.83 to -1.48) with a mean value of -0.76 (-1.1) over New Mexico (Gardner et al., 1998). The vertical wind has the frequency spectrum indices of -0.8 to -0.9 in the troposphere and -0.6 to -0.7 in the lower stratosphere, and the vertical wavenumber spectrum index of -1.27 in the troposphere and lower stratosphere from the sounding system (SOUYS) very high frequency (VHF) radar data (Larsen et al., 1987). And the similar slopes in the upper troposphere and lower stratosphere are presented in the Arecibo ultra-high-frequency radar data (Cornish, 1988). The middle and upper

atmosphere radar observation shows an average frequency spectrum slope of about -0.4 in the vertical wind in the lower troposphere (Y. Yamamoto et al., 1996). However, a detailed analysis of the vertical wind from the SOUSY-VHF Radar indicates that the slope of frequency (vertical wavenumber) spectrum displays significant dependence on height with a variational range of -2.2 to 0 (-1.67 to -0.34) in 2 – 16 km (Kuo et al., 1985). The slope of frequency spectrum in the troposphere and lower stratosphere from the middle atmosphere Alomar radar system and multifrequency atmospheric radar is inferred to be about $-5/3$ in the strong winds (Q. Li et al., 2018; Muschinski et al., 2001), and steeper values of -3 to -4 by Muschinski et al. (2001) but shallower values of around -1 by Q. Li et al. (2018) in the weak winds. The slope of vertical wavenumber spectrum has the mean value of -2.2 in the troposphere and lower stratosphere from the Gadanki mesosphere–stratosphere–troposphere (MST) radar measurement (Dutta et al., 2005). The vertical wind perturbation derived from radiosonde ascent rate change is reported to have the wavenumber spectrum indices of -1.1 to -0.2 in the troposphere and -0.6 to -0.1 in the lower stratosphere (S. D. Zhang et al., 2017). Hence, the spectral slope of the vertical wind shows obvious difference from one to another observations. Because of the difficulty of detecting the vertical wind, the change of spectral slope may be due to the relatively large uncertainty in the vertical wind velocity resulting from the radar beam width and beam pointing zenith and azimuth deviation in radar measurement since the vertical wind is roughly 1–2 orders smaller than the horizontal winds, and from the ascent rate perturbation of balloon treated as the vertical velocity perturbation in radiosonde observation now that radiosonde does not directly sound the vertical wind. Many studies indicate that the vertical wind should obey distinctive spectral laws comparing to the horizontal winds and temperature. Hence, it is of significance to extensively obtain the fine precision vertical wind and reveal the general characteristic of the vertical wind spectra.

Lidar is one of a very few systems that can measure the vertical wind, especially in the MLT with high temporal resolution. Lidar observation provides an opportunity to study and compare the features of three-dimensional wind and temperature spectra. In this paper, we use the lidar data to investigate the GW activity and their spectral features. In Section 2, the data used are briefly described. In Section 3, an estimate of quasi-monochromatic IGW in the lidar data is presented in detail, and then statistical characteristics of IGWs in the MLT are investigated based on 27-night observations. The three-dimensional wind and temperature spectra are discussed in Section 5. Finally, a summary is provided in Section 6.

2. Lidar Data

The three-dimensional winds and temperature measured by the Na lidar at Andes Lidar Observatory (ALO) in Cerro Pachón, Chile (30.25°S , 70.74°W), are used to investigate the GWs and their spectral characteristics. The design architecture and performance specifications of the ALO lidar system are described in detail by A. Z. Liu et al. (2016). The lidar system has about 0.4 – 0.6 W m^2 power aperture product and employs the three-frequency technique to measure the line-of-sight wind, temperature, and Na number density (She & Yu, 1994). The line-of-sight wind and temperature are derived based on the ratios among the backscattered signals at these three frequencies and their errors are estimated by photon noise (Krueger et al., 2015). The wind and temperature were derived from 500 m and 1 min photon echo signal and then smoothed with 1 km and 15 min full-width hamming windows, which leads to temporal and spatial resolutions of about 0.5 km and 6 min in the observational data. The uncertainty in temperature is typically about 0.5 K around 90 km and increase to roughly 1.5 K around 85 km and 2–3 K around 100 km. The uncertainty in the horizontal winds has the values of approximately 2 m s^{-1} around 90 km and 4–5 (8–10) m s^{-1} around 85 (100) km.

The continuous measurement of 10.6 h from 2306 UT, April 18, 2015 to 0942 UT, April 19, 2015, is utilized to investigate the dominant IGW activity in the night, especially in the vertical wind, showing that the clear wave activity can be observed in the vertical wind from the lidar. Next, we statistically study the wave activities and their frequency and vertical wavenumber spectra. For the fine resolutions of frequency and wavenumber spectra, we choose the data that meet the continuous observation longer than 8 h and spatial coverage larger than 17 km in all the temperature and wind field, and then 27-night observations are selected. The data are obtained from 1, 2, 3, 1, and 3 nights in January, April, July, October, and November 2015; 3, 4, 5, and 3 nights in February, March, October, and November 2016; and 2 nights in April 2017, respectively.

3. IGW Analysis

3.1. IGW Case Study

Figure 1 shows the zonal (u , positive eastward), meridional (v , positive northward), and vertical (w , positive upward) winds and temperature (T) from 84.5 to 101.5 km observed by the Na lidar at ALO from 2306 UT, April 18, 2015. In order to extract the dominant GW from the lidar data and reduce the influence of large-scale or long-period perturbations on GW analysis (Huang et al., 2017), we fit and subtract a second-order polynomial with respect to time from the observations at each altitude. For the calculated results, we fit and subtract a second-order polynomial with respect to altitude again to obtain the total wave perturbations, which are also depicted in Figure 1. A predominant quasi-monochromatic GW with downward phase propagation can be seen in all the perturbation fields. In the vertical wind, there are more short period perturbations relative to the zonal and meridional winds and temperature, which is consistent with the feature of the vertical wind that it is more sensitive to high frequency waves according to the polarization relations of GWs (Fritts & Alexander, 2003). Even so, the predominant GW can clearly be distinguished from the perturbation fields. Hence, it can be inferred that an upward propagating GW, with downward phase progression, is observed by the lidar in this night.

We make a Lomb–Scargle spectrum analysis (Scargle, 1982), with a four-time oversampling, on the perturbation fields to estimate the temporal and vertical scales of the dominant wave. Figure 2 shows the frequency and vertical wavenumber spectra in the three-dimensional winds and temperature. The vertical line denotes a period of 6.1 h in the frequency spectrum and a vertical wavelength of 9.7 km in the wavenumber spectrum, thus the predominant quasi-monochromatic GW has the period of about 6.1 h and the vertical wavelength of roughly 9.7 km since the two strong spectral peaks appear in all the four components. We treated the long-period GW as a lower frequency IGW and will estimate the feasibility based on the wave intrinsic period. In addition, an obvious spectral peak at a period of 3.5 h occurs only in the vertical wind and temperature at about 85–90 km, and the corresponding perturbation can be seen in Figures 1g and 1h. In that case, we focus only on the IGW and estimate its propagation features.

We extract the zonal wind, meridional wind, and vertical wind and temperature perturbation components (u' , v' , w' , T') of the IGW from their total perturbation fields by making a sinusoidal wave fit under a period of 6.1 h, and then use the hodograph technique to determine the horizontal propagation direction of the upward moving IGW. Previous studies showed that only the direction of the hodograph ellipse remains relatively constant, while the intrinsic frequency estimated from the ratio of the ellipse major and minor axes varies dramatically at different times or altitudes (Chen et al., 2013; F. Zhang et al., 2004). By combining the IGW polarization relation with the Doppler shift equation, the intrinsic frequency and horizontal wave length can be calculated in a more accurate way after the horizontal direction is determined (Chen et al., 2013; Huang et al., 2017). This method is applied in this study. The polarization relation derived from the linear wave theory is written as follows (Fritts & Alexander, 2003):

$$\frac{\tilde{u}}{\tilde{v}} = i \frac{\Omega}{f} \quad (1)$$

where \tilde{u} and \tilde{v} are the horizontal wind perturbation in the direction of propagation and the perpendicular counterpart, respectively; i is the imaginary unit, representing a quarter cycle out of phase; Ω is the intrinsic wave frequency; and the inertia frequency is $f = -7.4 \times 10^{-5} \text{ rad s}^{-1}$ at 30.25°S. Because the $u'-v'$ hodograph has the same rotation direction as the $\tilde{u}-\tilde{v}$ hodograph, the $u'-v'$ hodograph is generally used to determine the wave propagation direction. In this case, the horizontal propagation direction of the IGW can be estimated by the major axis direction of the $u'-v'$ hodograph ellipse, but with a 180° ambiguity (Gavrilov et al., 1996), and then the polarization relation between the horizontal wind perturbation \tilde{u} and temperature perturbation T' can be used to resolve the 180° ambiguity (Hu et al., 2002; T. Li et al., 2007):

$$\frac{T'}{\tilde{u}} = \frac{H(ik_z + 1/2H)(\Omega^2 - f^2)}{R\Omega k_h} \quad (2)$$

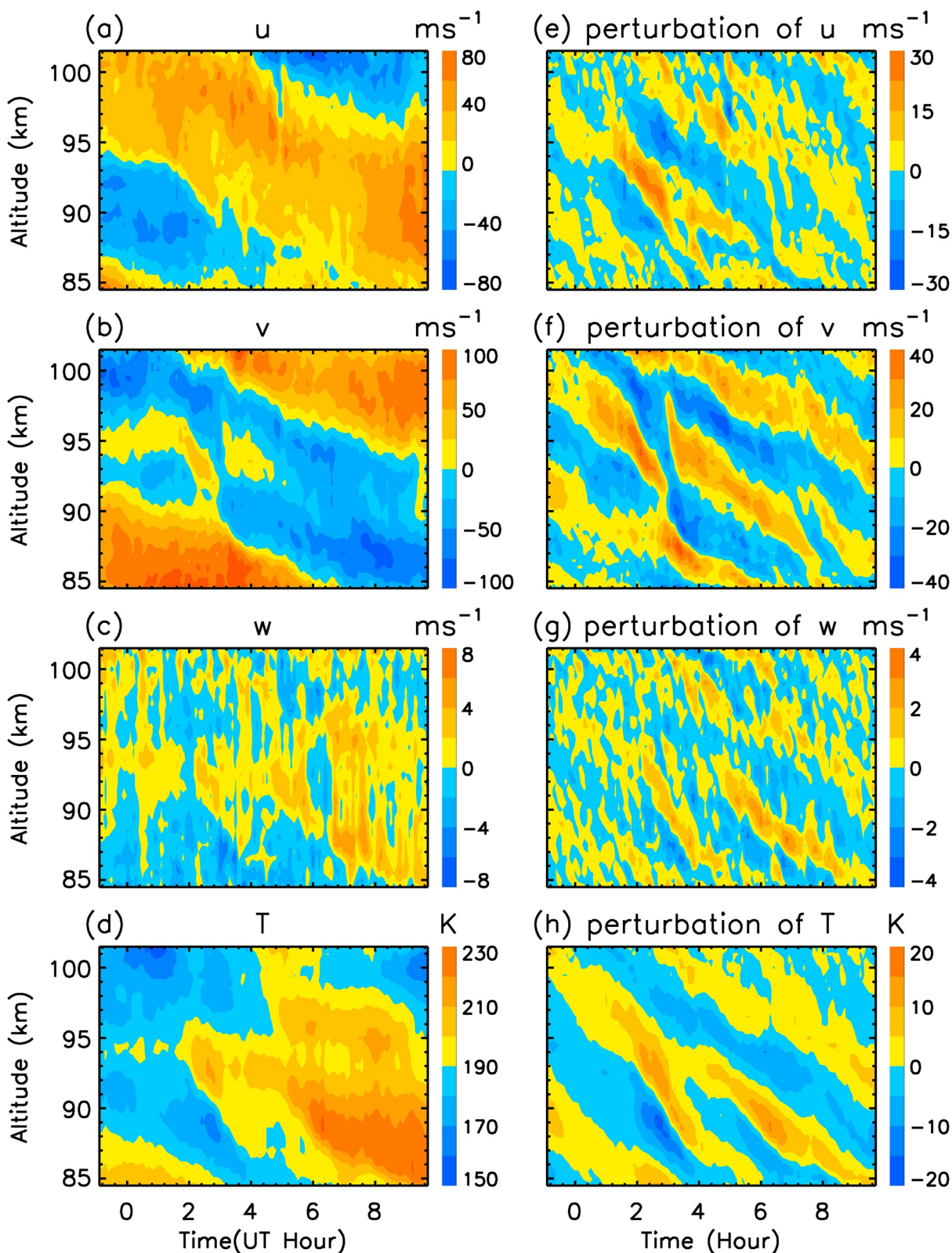


Figure 1. (a, e) Zonal wind, (b, f) meridional wind, (c, g) vertical wind, and (d, h) temperature and their total perturbations at 84.5–101.5 km measured by lidar for 10.6 h from 2306 UT, April 18, 2015. The left column denotes the observed values, and the right column denotes the corresponding perturbations.

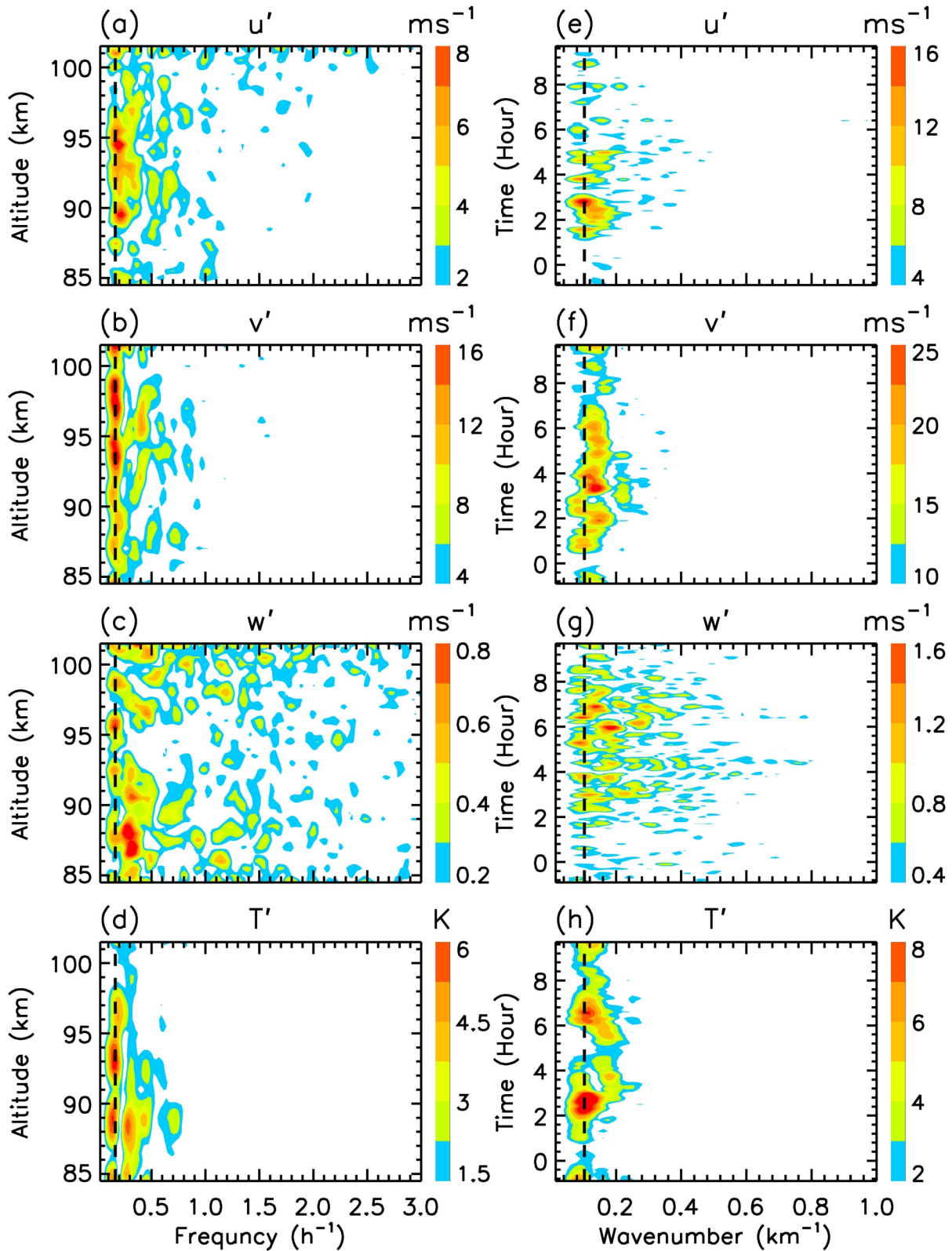


Figure 2. Lomb–Scargle frequency and vertical wavenumber spectra of (a, e) zonal wind, (b, f) meridional wind, (c, g) vertical wind, and (d, h) temperature perturbations. The left and right columns denote the frequency and wavenumber spectra, respectively. The dashed vertical line in the frequency and wavenumber spectra corresponds to a period of 6.1 h and a wavelength of 9.7 km, respectively.

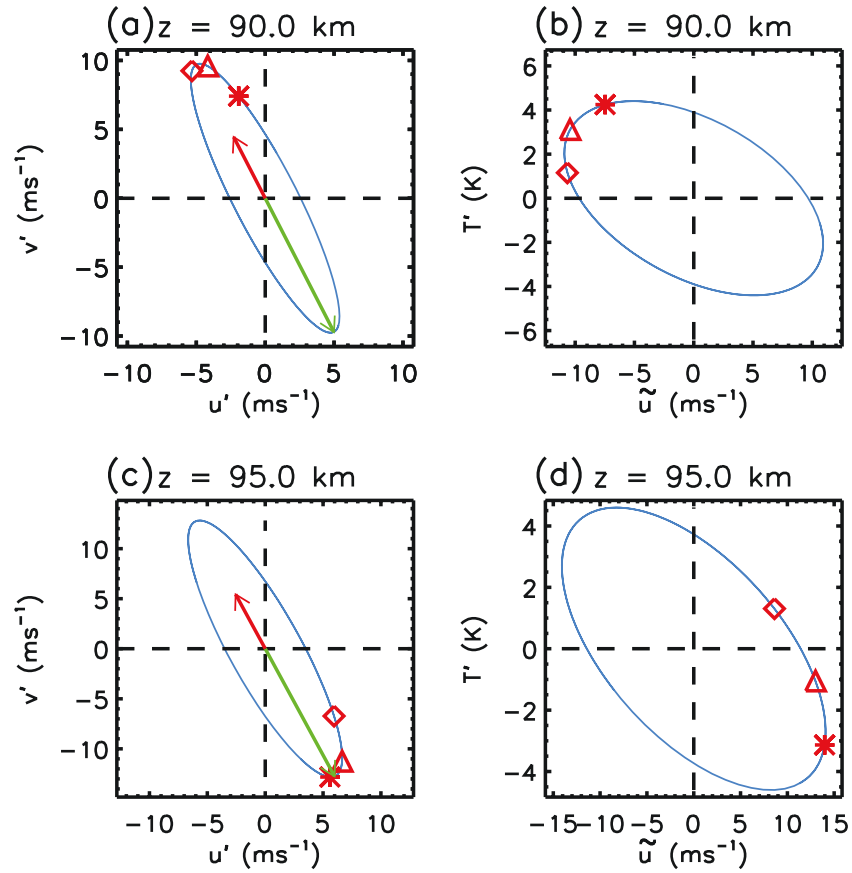


Figure 3. Temporal hodographs at (a, b) 91 km and (c, d) 96 km. The left column represents the hodograph of zonal and meridional wind perturbations, and the right column represents the hodograph of temperature perturbation and horizontal wind perturbation in assumed propagation direction. The star, triangle, and square are at 0, 1, and 2 h, respectively. The green arrow along the major axis of ellipse denotes the assumed propagation direction of the IGW, and the red arrow denotes the actual propagation direction.

where k_h is the horizontal wavenumber; k_z is the vertical wavenumber; H is the scale height; and R is the atmospheric gas constant. \tilde{u} is calculated by projecting the zonal and meridional wind perturbations onto the assumed horizontal propagation direction along the ellipse major axis. According to Equation 2, the $\tilde{u} - T'$ hodograph should rotate clockwise for an upward propagating wave. Otherwise, the horizontal propagation direction is opposite to the assumed propagation direction.

Based on the fitted wave perturbation components, we plot the temporal hodographs at 90 and 95 km, which is shown in Figure 3. In Figures 3a and 3c, the $u' - v'$ hodographs rotate counterclockwise, and the major axis of the two polarization ellipses shows a nearly same direction. We choose a direction of major axis as the horizontal propagation direction of wave, which is denoted by the green arrow. The chosen direction is about 73° and 78° south of east at 90 and 95 km, respectively, and its averaged value of 73.8° between 84.5 and 101.5 km is treated as the wave propagation direction. The $\tilde{u} - T'$ hodograph at 90 and 95 km in Figures 3b and 3d shows a counterclockwise rotation, indicating that the wave propagation is opposite to the assumed direction, thus the horizontal propagation direction is 26.2° west of north, represented by the red arrow in Figures 3a and 3c.

We estimate the intrinsic frequency and horizontal wavenumber by solving the following dispersion relation and Doppler shift equation (Fritts & Alexander, 2003; H.-L. Liu & Meriwether, 2004):

$$k_h^2 = \frac{\Omega^2 - f^2}{N^2} \left(k_z^2 + \frac{1}{4H^2} \right) \quad (3)$$

$$\Omega = \omega - k_h U \quad (4)$$

where N is the buoyancy frequency; ω is the ground-based wave frequency; and U is the horizontal background wind obtained by projecting the zonal and meridional background winds to the horizontal propagation direction of IGW. We roughly estimate the background parameter values by simply calculating their averages over the whole time and space domain. The zonal and meridional background winds are calculated to be 9.1 and -4.5 m s^{-1} , respectively, thus the horizontal background wind is derived to be -6.7 m s^{-1} based on the wave propagation direction of 26.2° counterclockwise from north. The scale height is $H = 5.8$ km, $k_z = 6.5 \times 10^{-4}$ rad s^{-1} is calculated from the vertical wavelength $\lambda_z = 9.7$ km, and the buoyancy frequency is $N = 2.1 \times 10^{-2}$ rad s^{-1} derived from the background temperature. According to Equations 3 and 4, the intrinsic frequency and the horizontal wavenumber are calculated to be $\Omega = 3.8 \times 10^{-4}$ rad s^{-1} and $k_h = 1.3 \times 10^{-5}$ rad m^{-1} , respectively, thus the IGW has an intrinsic period $T_\Omega = 4.7$ h and a horizontal wavelength $\lambda_h = 484$ km. The intrinsic period of 4.7 h is far larger than the buoyancy oscillation period of about 5 min and is one fifth of the inertial oscillation period. In the statistical investigation of IGWs, one tenth of the inertial period is relatively widely chosen as the lower limit of IGWs (Hall et al., 1995; Hamilton, 1991; Hirota & Niki, 1985; Qing et al., 2014; Vincent & Alexander, 2000; Wang et al., 2005; Yoshiki et al., 2004; S. D. Zhang & Yi, 2005, 2007). The observed GW with $\Omega = 5f$ is regarded as an IGW, which causes some error, whereas the discrepancy may not be very serious, and the hodograph may still help us roughly estimate the horizontal propagation direction of wave. Accordingly, the absolute values of zonal and meridional wavenumbers calculated to be 5.74×10^{-6} and 1.17×10^{-5} rad m^{-1} , corresponding to the zonal and meridional wavelengths of about 1,095 and 539 km, respectively.

Wave kinetic (E_k) and potential (E_p) energies represent the magnitude of wave activity. The kinetic and potential energies per unit mass are expressed as (Huang et al., 2018; S. D. Zhang & Yi, 2007)

$$E_k = \frac{1}{2} \left(\overline{u'^2} + \overline{v'^2} + \overline{w'^2} \right) \quad (5)$$

$$E_p = \frac{g^2}{2N^2} \overline{\hat{T}'^2} \quad (6)$$

where $\hat{T}' = T' / \bar{T}$ is the relative temperature perturbation, defined as the ratio of the temperature perturbation $T'(z)$ to the mean temperature $T_0(z)$; $g = 9.77$ m s^{-2} is the gravitational acceleration; and the overbar denotes an average over the height range. In this way, the kinetic and potential energies of the IGW are $E_k = 82.8$ J/kg and $E_p = 71.8$ J/kg derived from Equations 5 and 6, and their ratio is 1.15. According to the linear wave theory, the ratio of IGW kinetic to potential energies can be written as (Collins et al., 1994; Yamamori & Sato, 2006)

$$\frac{E_k}{E_p} = \frac{\Omega^2 + f^2}{\Omega^2 - f^2} \quad (7)$$

here, $\Omega = 5f$, E_k/E_p is calculated to be 1.08, which is approximately consistent with the value of 1.15 derived from the realistic wave energies. The consistency indicates that the IGW in the MLT shows the feature of freely propagating wave far from its excitation region.

3.2. Statistical Characteristics of IGWs

We choose 27-night lidar data with observation time exceeding 8 h and effective observation height range larger than 17 km, to statistically analyze the general characteristics of IGWs in the MLT. In order to reduce the error in the estimate, we set $\Omega \leq 5f$ as a criterion of IGWs in our investigation, which is more restrictive than that of $\Omega < 10f$ used relatively extensively in previous studies (Hall et al., 1995; Hamilton, 1991; Qing et al., 2014; Vincent & Alexander, 2000; Wang et al., 2005; Yoshiki et al., 2004; S. D. Zhang & Yi, 2005, 2007). There are two nights (in October 2016 and April 2017) in which the dominant wave does not meet the criterion, thus we extract 25 IGWs for the analysis.

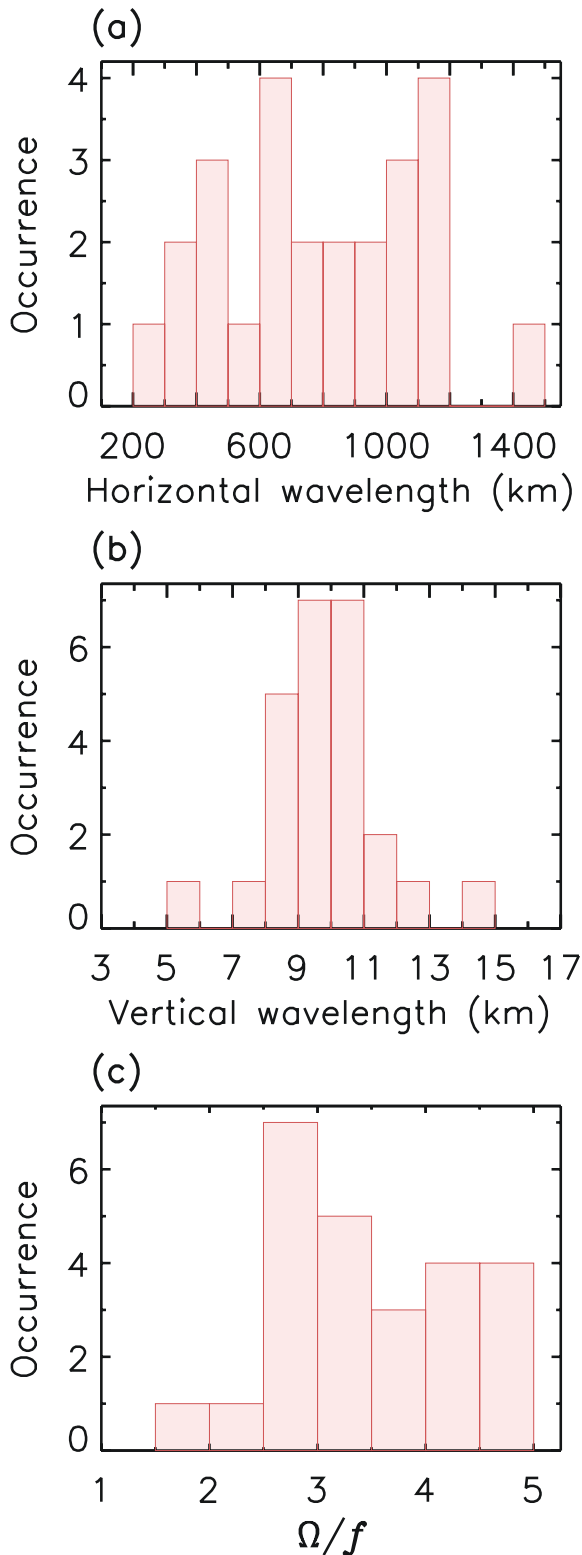


Figure 4. Distribution of (a) horizontal and (b) vertical wavelengths and (c) Ω/f for 25 IGWs observed by lidar. IGW, inertia-gravity wave.

Figures 4a and 4b depict the distribution of the horizontal and vertical wavelengths. In all the 25 IGWs, the horizontal wavelength is between 200 and 1,500 km, and the vertical wavelength changes from 5 to 15 km. These wavelengths are in the typical scale range of IGWs. Even so, the horizontal (vertical) wavelength has the mean value of 788.7 (9.8) km and a nearly equal median value of 782.8 (9.7) km, which are slightly larger than those in some previous studies. Based on the profiles observed by radiosonde, the IGWs are commonly extracted in the tropospheric segment and the lower stratospheric segment with a height range of less than 10 km, respectively, in order to avoid the influences of extremely low temperature around the tropopause and very large zonal wind in the tropospheric jet. At midlatitudes, although there are the IGWs with the horizontal scale of over 2,000 km, the mean horizontal and vertical wavelengths are generally about 200–600 km and 2–6 km (Plougonven et al., 2003; Wang et al., 2005; S. D. Zhang & Yi, 2005, 2007; Zink & Vincent, 2001), respectively. And the calculated mean wavelength is generally sensitive to the chosen height range that larger the vertical range is, longer the dominant IGW wavelength is. In our study, the height coverage is at least 17 km, thus the larger scale waves are observed relative to the previous results. Based on the horizontal wind measurements by MST radar at midlatitudes, the IGWs at the tropospheric heights of 3–10 km are reported to have the horizontal and vertical wavelengths of 100–1,500 km and 1.5–5.5 km, with the mean values of 469 and 3.8 km (Qing et al., 2014), respectively, and the mean horizontal and vertical wavelengths are about 1,000 and 3 km around the tropopause region (Nastrom & Eaton, 2006). In the MLT, the lidar data between 84 and 104 km show the averaged horizontal and vertical scales of 1,360 and 12.2 km for the IGWs over the midlatitudes (Hu et al., 2002). The past case studies also report obvious different scale GWs in the lidar observations, for example, the waves of ($\lambda_h = 2,200$ km, $\lambda_z = 22$ km, $T_\Omega = 7.9$ h) by Chen et al. (2013), ($\lambda_h = 1,230$ km, $\lambda_z = 17.3$ km, $T_\Omega = 2.5$ h) by Cai et al. (2014), ($\lambda_h = 219$ km, $\lambda_z = 16$ km, $T_\Omega = 1.3$ h) by Lu et al. (2015), and ($\lambda_h = 85$ km, $\lambda_z = 4.1$ km, $T_\Omega = 1.7$ h) by Kwon and Gardner (1990). As shown above, owing to the IGWs extracted from the large vertical range in the lidar measurements, the dominant waves generally have larger wavelengths relative to those in the radiosonde and MST radar observations. At the same time, by virtue of the fine resolution of lidar observations, the lidar data are also used to study the high- and medium-frequency GWs and GW breakdown (Cai et al., 2014; Lu et al., 2017).

Figure 4c shows the occurrence of the intrinsic frequency. The mean and median intrinsic frequencies are $3.47f$ and $3.24f$, corresponding to the intrinsic periods of 7.4 and 7.5 h, respectively, and almost half intrinsic frequency lies in $2.5f$ – $3.5f$. The distribution of Ω/f is roughly consistent with previous results at midlatitudes that the intrinsic frequencies of IGWs are mainly distributed between $2f$ and $4f$ (Hu et al., 2002; Qing et al., 2014; Wang et al., 2005; S. D. Zhang & Yi, 2005, 2007). It is interesting that the intrinsic frequency distribution displays the similarity in the different layers observed by different instruments though there are some statistical differences in the wavelengths of IGWs. All 25 IGWs propagate upward in the vertical direction, and their horizontal propagation is shown in Figure 5. The IGWs in the MLT over Andes evidently exhibit the preferential propagation in the meridian direction relative to in the zonal direction. The anisotropy in the wave propagation direction is exten-

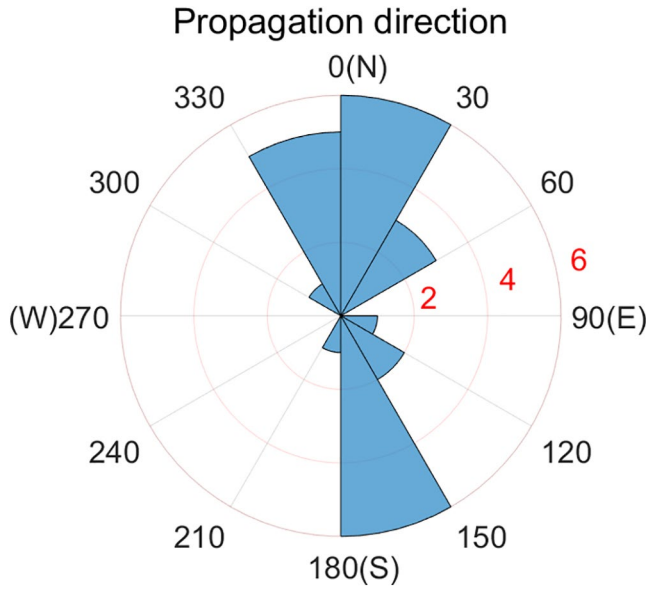


Figure 5. Distribution of horizontal propagation direction for 25 IGWs observed by lidar. IGW, inertia-gravity wave.

sively reported at different latitudes (Hu et al., 2002; Huang et al., 2018; Moffat-Griffin et al., 2011; Vincent & Alexander, 2000; Yamamori & Sato, 2006; Yoshiki et al., 2004), which is generally attributed to the wave excitation process and propagation effect.

Figure 6a depicts the total wave energy and the ratio of kinetic to potential energies. These waves in the MLT have the mean energy of 92.2 J kg^{-1} , which is obviously larger than those observed in the troposphere and stratosphere (Moffat-Griffin et al., 2011; Ratnam et al., 2008; Vincent & Alexander, 2000; S. D. Zhang & Yi, 2005, 2007) because the waves propagating to the MLT generally have large amplitudes due to the exponentially decreasing atmospheric density with height. Figure 6b illustrates that the ratio of kinetic to potential energies derived from the lidar observation is in nearly agreement with Equation 7. This indicates that the waves extracted in the condition of $\Omega \leq 5f$ can meet the linear theory of IGWs and show the characteristic of freely propagating waves.

4. Frequency and Wavenumber Spectra of GWs

4.1. Observation in One Night

In this section, we investigate the PSDs of frequency and wavenumber spectra for the zonal wind, meridional wind, vertical wind, and relative temperature perturbation observed in the night of April 18–19, 2015.

The frequency PSD $F(\omega_k)$ is calculated by using the Fourier spectrum $f(\omega_k)$ derived from discrete Fourier transform for the corresponding perturbation time series $x(t_j)$ at each height, which can be written as follows (Dewan & Grossbard, 2000):

$$F(\omega_k) = \Delta t(n-1) \left| f(\omega_k) \right|^2 = \Delta t(n-1) \left| \frac{1}{n} \sum_{j=0}^{n-1} x(t_j) e^{-i \frac{2\pi \omega_k}{n} j} \right|^2 \quad (8)$$

where the temporal resolution $\Delta t = 0.1 \text{ h}$; n is the total number of data; and ω_k is the k th frequency. The frequency spectrum at each observational height is calculated individually and then averaged to obtain the mean spectrum. The spectral slope is determined by applying a linear fit to the mean spectrum in a logarithmic coordinate. Figure 7 presents the frequency spectra of the zonal wind, meridional wind, vertical wind, and relative temperature perturbations observed by the lidar in this night. The PSDs in the zonal wind, meridional wind, and temperature have the spectral slopes of -1.5 , -1.9 , and -2.1 , respectively, and these spectral slopes are close to the universal spectrum index of $-5/3$ in the spectral theories. Although the peak amplitude of PSDs is on the order of $\sim 10^6 \text{ m}^2 \text{ s}^{-2} \text{ Hz}^{-1}$ in the horizontal winds, the meridional wind has a larger peak amplitude relative to the zonal wind because the dominant IGW has a stronger perturbation in the meridional wind field than in the zonal wind field, as shown in Figures 1–3. The spectra shape of the vertical wind can be distinguished from the other three components. The vertical wind has a spectral slope of -1.1 , which is significantly shallower than the canonical value of $-5/3$ in the horizontal winds and temperature, and a peak amplitude with the order of $\sim 10^3 \text{ m}^2 \text{ s}^{-2} \text{ Hz}^{-1}$, being about 3 orders smaller than that in the horizontal winds because the horizontal wind perturbations are generally 1–2 orders larger in comparison with the vertical wind perturbation.

We use the similar method following Equation 8 to calculate the PSDs of vertical wavenumber spectra for these four perturbations in each observational profile. The vertical wavenumber spectra of the zonal wind, meridional wind, vertical wind, and relative temperature perturbations at different observational times and their averaged and fitted results are also shown in Figure 7. The vertical wavenumber spectrum has the slope of -2.6 in the temperature close to the canonical value of -3 and less negative slopes of -1.6 and -2.1 in the zonal and meridional winds, respectively. The spectral shape of the vertical wind is slightly different from that of the other three components. Relative to the horizontal winds and temperature, the

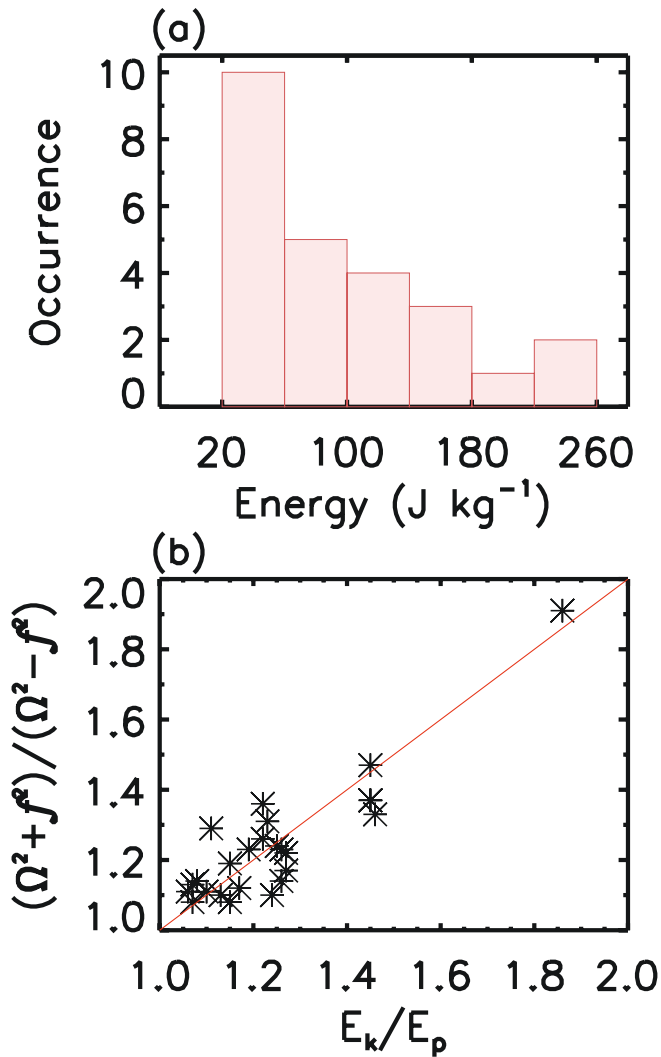


Figure 6. (a) Total energy distribution and (b) ratio of kinetic to potential energies for 25 IGWs observed by lidar. In (b), the horizontal axis denotes the ratio value derived from the wave energies observed by the lidar, and the vertical axis denotes the ratio value derived from the linear theory of IGWs. IGW, inertia-gravity wave.

as the unsaturated spectrum region. It can be noted from Figures 8c and 8g that both the frequency and wavenumber spectra in the vertical wind show a steeper spectral tail, which is clearly distinguished from the saturated spectrum region, but a similar spectral tail does not occur in the zonal and meridional winds. The steeper tail of wavenumber spectrum in the vertical wind also clearly appears in the radiosonde observation by S. D. Zhang et al. (2017). We refit the saturated spectrum and spectral tail of the vertical wind. The fitted spectral index is -0.4 and -1.1 in the saturated frequency and wavenumber spectra, respectively, thus the vertical wind has much shallower indices of saturated frequency and wavenumber spectra than the horizontal winds. Meanwhile, in the spectral tail regions, corresponding to 0.2–0.4 h periods and 1–1.7 km vertical scales, the fitted frequency and wavenumber spectrum slopes of -2.2 and -3.5 are far steeper than the saturated spectrum indices of -0.4 and -1.1 , respectively. Both the steeper spectrum tails indicate a more intense dissipation of the vertical wind perturbation in the small temporal and spatial scales. The obvious differences between the vertical and horizontal wind spectra imply that the vertical wind may obey the different spectral laws from the zonal and meridional winds.

vertical wind has smoother spectral amplitudes around the peak value and a steeper spectral tail at the small scales, indicating that the vertical wind perturbation is more sensitive to the high frequency waves. The fitted spectrum index is -1.7 in the vertical wind, and the peak amplitude is about 2–3 orders smaller than in the horizontal winds.

4.2. Statistical Feature of Spectra

We choose 27-night lidar data with observation time exceeding 8 h and effective observation height range larger than 17 km, to statistically analyze the general feature of frequency and vertical wavenumber spectra in the MLT. Figure 8 presents the averaged frequency and vertical wavenumber spectra of the zonal wind, meridional wind, vertical wind, and relative temperature perturbations observed in the 27 nights.

In Figure 8, the blue and red lines denote the averaged frequency spectrum and linearly fitted spectrum. The feature of the statistical frequency spectrum is similar to that in the case analysis above. The peak amplitude of frequency spectrum is the order of $\sim 10^6 \text{ m}^2 \text{ s}^{-2} \text{ Hz}^{-1}$ in the zonal and meridional winds, $\sim 10^3 \text{ m}^2 \text{ s}^{-2} \text{ Hz}^{-1}$ in the vertical wind, and $\sim 10 \text{ Hz}^{-1}$ in the temperature, respectively. The fitted spectral slopes of -1.4 , -1.7 , and -2.3 in the zonal and meridional winds and temperature vary around the saturated spectrum index of $-5/3$, respectively, while the frequency spectrum of the vertical wind has a less negative slope of -0.8 . The averaged PSDs and fitted slopes of wavenumber spectra in Figure 8 exhibit the nearly same peak amplitudes and spectral indices as the case results shown in Figure 7. The peak amplitude of wavenumber spectrum is the order of $\sim 10^3 \text{ m}^2 \text{ s}^{-2} \text{ km}$ in the zonal and meridional winds, $\sim 10 \text{ m}^2 \text{ s}^{-2} \text{ Hz}^{-1}$ in the vertical wind, and $\sim 10^{-2} \text{ km}$ in the temperature, respectively. The spectral slope of -2.6 in the relative temperature perturbation is close to the saturated spectrum index of -3 ; however, the statistical slopes of -1.5 and -2.0 in the zonal and meridional winds indicate that a less negative index in the horizontal winds may be a general phenomenon in the MLT over Andes. In the same spectrum range, the fitted slope in the vertical wind is -1.6 , which is approximately consistent with those in the horizontal winds.

In the saturated spectrum theory, the spectrum part on the right of the peak amplitude within the GW scales is generally referred to as the saturated spectrum region, and the low-frequency or wavenumber part on the left of the peak amplitude with a positive slope is regarded

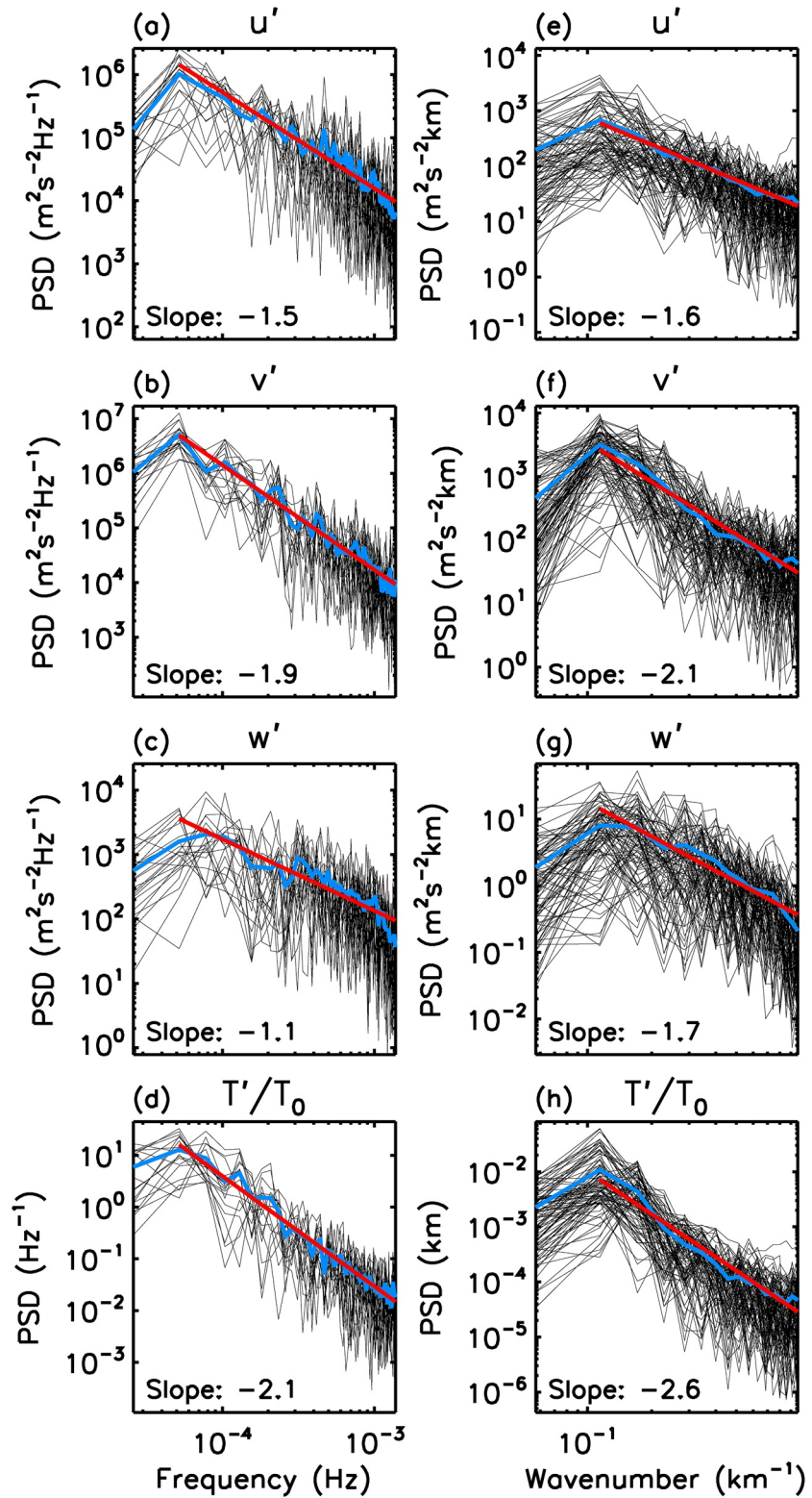


Figure 7. PSDs of frequency and wavenumber spectra in (a, e) zonal wind, (b, f) meridional wind, (c, g) vertical wind, and (d, h) relative temperature perturbations observed in night of April 18–19, 2015. The left and right columns denote the frequency and wavenumber spectra, respectively. The black and blue lines denote the PSD at each altitude and their averaged value, respectively, and the red line denotes the linearly fitted value of the averaged PSD. PSD, power spectral density.

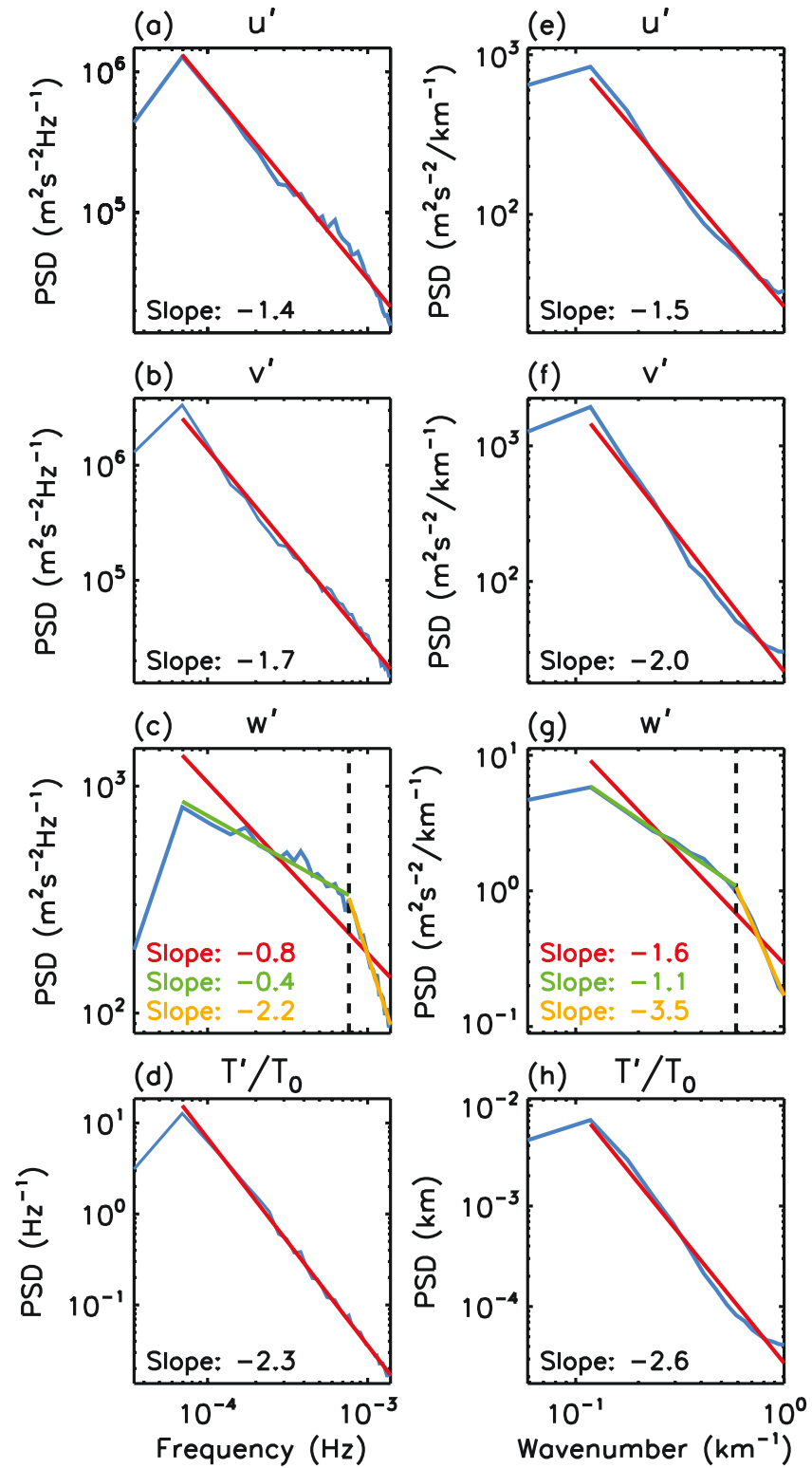


Figure 8. Averaged PSDs of frequency and wavenumber spectra and their fitted values for (a, e) zonal wind, (b, f) meridional wind, (c, g) vertical wind, and (d, h) relative temperature perturbations observed in 25 nights. The left and right columns denote the frequency and wavenumber spectra, and the blue and red lines denote the averaged PSD and fitted value, respectively. In (c) and (g), the green and yellow lines denote the fitted PSDs in the saturated spectrum and steep spectral tail regions of the vertical wind, respectively. PSD, power spectral density.

In addition, both the case and statistical analyses show that peak amplitudes of frequency and wavenumber spectra in the meridional wind are larger than in the zonal wind. This is related to the ratio of the IGW zonal wavenumber to meridional wavenumber, or the IGW horizontal propagation direction. According to the polarization relation (Fritts & Alexander, 2003), for a constant intrinsic frequency IGW, the larger the meridional wavenumber is relative to the zonal wavenumber, the stronger the meridional wind amplitude is relative to the zonal wind amplitude. In the observation during the night of April 18–19, 2015, the predominant IGW propagates along the direction of 26.2° counterclockwise from north, leading to that the meridional wavenumber is about twice as large as the zonal wavenumber based on horizontal wave vector decomposition, thus the wave amplitude and spectral peak amplitude are evidently stronger in the meridional wind than in the zonal wind. As shown in Figure 5, relative to in the zonal direction, the preferential propagation in the meridional direction is the general feature of the IGWs in the MLT over Andes, thus the statistical spectrum has larger peak amplitude and then steeper slope in the meridional wind than in the zonal wind, as shown in Figure 8. We speculate that the preferential propagation direction is possibly connected with the influence of the nearly north-south Andes mountain on the wave generation or the effect of the background wind on the wave propagation.

5. Summary

In this work, we use the lidar observation to study the features of GW activities and their spectra in the MLT over Andes. The 10.6 h lidar observation displays a predominant IGW with clearly downward phase progression in the three-dimensional winds and temperature. The Lomb–Scargle spectrum analysis and hodograph technique show that the predominant wave has a ground-based period of 6.1 h and a vertical wavelength of 9.7 km and propagates along the horizontal direction of 26.2° counterclockwise from north. The horizontal wavelength is calculated to be 484 km, and the intrinsic wave period is about 4.7 h because the wave travels against the background wind of 6.7 m s^{-1} . Owing to the horizontal propagation direction close to the meridional direction, the horizontal wave vector has a larger projection in the meridian direction than in the zonal direction, thus the meridional wavenumber is larger relative to the zonal wavenumber. According to the GW polarization relation, the amplitude is stronger in the meridional wind than in the zonal wind, as shown in the Lomb–Scargle spectrum and PSDs of the zonal and meridional winds.

In the 27-night observations, 25 IGWs are extracted. Their horizontal and vertical wavelengths are in the ranges of 200–1,500 km and 5–15 km, with the mean values of 788.7 and 9.8 km, respectively, and their intrinsic frequencies have the mean value of $3.47f$, corresponding to the intrinsic period of 7.4 h, thus these period and wavelength are the typical temporal and spatial scales of IGWs at midlatitudes. The wave energy is larger than that in the troposphere and stratosphere because the waves propagating to the MLT generally have high amplitudes. The ratio of kinetic to potential energies derived from the lidar observation closely agrees with the linear theory of IGWs, indicating that the IGWs in the MLT have the feature of freely propagating waves far from their excitation region. Similar to the case study, the statistical investigation shows that the IGWs in the MLT over Andes have the preferential propagation in the meridian direction relative to in the zonal direction. This causes stronger peak amplitude and steeper spectral slope in the meridional wind than in the zonal wind.

The statistical PSDs in the 27-night observations are nearly consistent with the PSDs in the night of April 18–19, 2015. The peak magnitudes of the zonal and meridional wind PSDs have the same orders of $\sim 10^6 \text{ m}^2 \text{ s}^{-2} \text{ Hz}^{-1}$ in the frequency spectrum and $\sim 10^3 \text{ m}^2 \text{ s}^{-2} \text{ km}$ in the vertical wavenumber spectrum though the maximum spectral amplitude is obviously stronger in the meridional wind compared with in the zonal wind. The PSD of frequency spectrum has the slopes of about -1.4 in the zonal wind, -1.7 in the meridional wind, and -2.3 in the relative temperature perturbation, and the spectral index of vertical wavenumber spectrum is about -1.6 in the zonal wind, -2.0 in the meridional wind, and -2.6 in the relative temperature perturbation. On the whole, the vertical wavenumber spectrum of the zonal wind has a relatively large deviation from the universal spectral index of -3 .

The spectral characteristic of the vertical wind is different from that of the other three components. The vertical wind has a steeper spectral tail in both the frequency and wavenumber spectra, which does not arise in the spectra of the horizontal winds and temperature. In the saturated spectrum region, the frequency and

vertical wavenumber spectrum slopes of -0.4 and -1.1 in the vertical wind are much shallower than those in the zonal and meridional winds and also than the canonical frequency and wavenumber spectrum indices of $-5/3$ and -3 , respectively. In the spectral tail region, the frequency and wavenumber spectrum slopes of -2.2 and -3.5 are far steeper than their saturated spectrum slopes, respectively. Hence, the vertical wind should obey the different spectral laws from the zonal and meridional winds.

Data Availability Statement

The lidar data in this study are available at the Andes Lidar Observatory database at <http://lidar.erau.edu/data/>.

Acknowledgments

We are grateful to the Editor and anonymous reviewers for their valuable comments on our paper. This work was jointly supported by the National Natural Science Foundation of China (through grants 41974176, 41674151, and 41531070).

References

- Acott, P. E., She, C.-Y., Krueger, D. A., Yan, Z.-A., Yuan, T., Yue, J., & Harrell, S. (2011). Observed nocturnal gravity wave variances and zonal momentum flux in mid-latitude mesopause region over Fort Collins, Colorado, USA. *Journal of Atmospheric and Solar-Terrestrial Physics*, 73, 449–456. <https://doi.org/10.1016/j.jastp.2010.10.016>
- Cai, X., Yuan, T., & Liu, H.-L. (2017). Large-scale gravity wave perturbations in the mesopause region above Northern Hemisphere mid-latitudes during autumnal equinox: A joint study by the USU Na lidar and Whole Atmosphere Community Climate Model. *Annales Geophysicae*, 35, 181–188. <https://doi.org/10.5194/angeo-35-181-2017>
- Cai, X., Yuan, T., Zhao, Y., Pautet, P.-D., Taylor, M. J., & Pendleton, W. R., Jr. (2014). A coordinated investigation of the gravity wave breaking and the associated dynamical instability by a Na lidar and an Advanced Mesosphere Temperature Mapper over Logan, UT (41.7°N, 111.8°W). *Journal of Geophysical Research: Space Physics*, 119, 6852–6864. <https://doi.org/10.1002/2014JA020131>
- Chen, C., Chu, X., McDonald, A. J., Vadas, S. L., Yu, Z., Fong, W., & Lu, X. (2013). Inertia-gravity waves in Antarctica: A case study using simultaneous lidar and radar measurements at McMurdo/Scott Base (77.8°S, 166.7°E). *Journal of Geophysical Research: Atmospheres*, 118, 2794–2808. <https://doi.org/10.1002/jgrd.50318>
- Chen, C., Chu, X., Zhao, J., Roberts, B. R., Yu, Z., Fong, W., et al. (2016). Lidar observations of persistent gravity waves with periods of 3–10 h in the Antarctic middle and upper atmosphere at McMurdo (77.83°S, 166.67°E). *Journal of Geophysical Research: Space Physics*, 121, 1483–1502. <https://doi.org/10.1002/2015JA022127>
- Collins, R. L., Nomura, A., & Gardner, C. S. (1994). Gravity waves in the upper mesosphere over Antarctica: Lidar observations at the South Pole and Syowa. *Journal of Geophysical Research*, 99(D3), 5475–5485. <https://doi.org/10.1029/93JD03276>
- Cornish, C. R. (1988). Observations of vertical velocities in the tropical upper troposphere and lower stratosphere using the Arecibo 430-MHz radar. *Journal of Geophysical Research*, 93(D8), 9419–9431. <https://doi.org/10.1029/JD093iD08p09419>
- Cot, C. (2001). Equatorial mesoscale wind and temperature fluctuations in the lower atmosphere. *Journal of Geophysical Research*, 106(D2), 1523–1532. <https://doi.org/10.1029/2000JD900597>
- Dewan, E. M., & Good, R. E. (1986). Saturation and the “universal” spectrum for vertical profiles of horizontal scalar winds in the atmosphere. *Journal of Geophysical Research*, 91(D2), 2742–2748. <https://doi.org/10.1029/JD091iD02p02742>
- Dewan, E. M., & Grossbard, N. (2000). Power spectral artifacts in published balloon data and implications regarding saturated gravity wave theories. *Journal of Geophysical Research*, 105(D4), 4667–4683. <https://doi.org/10.1029/1999JD901108>
- Dutta, G., Bapiraju, B., Prasad, T. S. P. L. N., Balasubrahmanyam, P., & Aleem Basha, H. (2005). Vertical wave number spectra of wind fluctuations in the troposphere and lower stratosphere over Gadanki, a tropical station. *Journal of Atmospheric and Solar-Terrestrial Physics*, 67(3), 251–258. <https://doi.org/10.1016/j.jastp.2004.08.003>
- Ern, M., Preusse, P., Alexander, M. J., & Warner, C. D. (2004). Absolute values of gravity wave momentum flux derived from satellite data. *Journal of Geophysical Research*, 109, D20103. <https://doi.org/10.1029/2004JD004752>
- Fritts, D. C., & Alexander, M. J. (2003). Gravity wave dynamics and effects in the middle atmosphere. *Reviews of Geophysics*, 41(1), 1003. <https://doi.org/10.1029/2001RG000106>
- Gardner, C. S. (1994). Diffusive filtering theory of gravity wave spectra in the atmosphere. *Journal of Geophysical Research*, 99(D10), 20601–20622. <https://doi.org/10.1029/94JD00819>
- Gardner, C. S., Franke, S. J., Yang, W., Tao, X., & Yu, J. R. (1998). Interpretation of gravity waves observed in the mesopause region at Starfire Optical Range, New Mexico: Strong evidence for nonseparable intrinsic (m , ω) spectra. *Journal of Geophysical Research*, 103(D8), 8699–8713. <https://doi.org/10.1029/97JD03428>
- Gardner, C. S., Tao, X., & Papen, G. C. (1995). Simultaneous lidar observations of vertical wind, temperature, and density profiles in the upper mesosphere: Evidence for nonseparability of atmospheric perturbation spectra. *Geophysical Research Letters*, 22(20), 2877–2880. <https://doi.org/10.1029/95GL02783>
- Gavrilov, N. M., Fukao, S., & Nakamura, T. (2000). Average statistical characteristics of long gravity waves observed with the middle and upper atmosphere radar in the mesosphere. *Journal of Geophysical Research*, 105(D7), 9365–9379. <https://doi.org/10.1029/1999JD901092>
- Gavrilov, N. M., Fukao, S., Nakamura, T., Tsuda, T., Yamanaka, M. D., & Yamamoto, M. (1996). Statistical analysis of gravity waves observed with the middle and upper atmosphere radar in the middle atmosphere: 1. Method and general characteristics. *Journal of Geophysical Research*, 101(D23), 29511–29521.
- Guharay, A., & Sekar, R. (2011). Seasonal characteristics of gravity waves in the middle atmosphere over Gadanki using Rayleigh lidar observations. *Journal of Atmospheric and Solar-Terrestrial Physics*, 73(13), 1762–1770. <https://doi.org/10.1016/j.jastp.2011.04.013>
- Guharay, A., Venkat Ratnam, M., Nath, D., & Dumka, U. C. (2010). Investigation of saturated gravity waves in the tropical lower atmosphere using radiosonde observations. *Radio Science*, 45, RS6008. <https://doi.org/10.1029/2010RS004372>
- Guo, Y., Liu, A. Z., & Gardner, C. S. (2017). First Na lidar measurements of turbulence heat flux, thermal diffusivity, and energy dissipation rate in the mesopause region. *Geophysical Research Letters*, 44, 5782–5790. <https://doi.org/10.1002/2017GL073807>
- Hall, G. E., Meek, C. E., & Manson, A. H. (1995). Hodograph analysis of mesopause region winds observed by three MF radars in the Canadian Prairies. *Journal of Geophysical Research*, 100(D4), 7411–7421. <https://doi.org/10.1029/95JD00195>
- Hamilton, K. (1991). Climatological statistics of stratospheric inertia-gravity waves deduced from historical rocketsonde wind and temperature data. *Journal of Geophysical Research*, 96(D11), 20831–20839. <https://doi.org/10.1029/91JD02188>

- Hickey, M. P., Huang, T.-Y., & Walterscheid, R. L. (2003). Gravity wave packet effects on chemical exothermic heating in the mesopause region. *Journal of Geophysical Research*, 108(A12), 1448. <https://doi.org/10.1029/2002JA009363>
- Hines, C. O. (1991). The saturation of gravity-waves in the middle atmosphere. 2. Development of Doppler-spread theory. *Journal of the Atmospheric Sciences*, 48(11), 1360–1379. [https://doi.org/10.1175/1520-0469\(1991\)048<1361:TSOGWI>2.0.CO;2](https://doi.org/10.1175/1520-0469(1991)048<1361:TSOGWI>2.0.CO;2)
- Hines, C. O. (1997). Doppler-spread parameterization of gravity-wave momentum deposition in the middle atmosphere. Part 1: Basic formulation. *Journal of Atmospheric and Solar-Terrestrial Physics*, 59(4), 371–386. [https://doi.org/10.1016/S1364-6826\(96\)00079-X](https://doi.org/10.1016/S1364-6826(96)00079-X)
- Hirota, I., & Niki, T. (1985). A statistical study of inertia-gravity waves in the middle atmosphere. *Journal of the Meteorological Society of Japan*, 63(6), 1055–1066. https://doi.org/10.2151/jmsj1965.63.6_1055
- Hoffmann, P., Becker, E., Singer, W., & Placke, M. (2010). Seasonal variation of mesospheric waves at northern middle and high latitudes. *Journal of Atmospheric and Solar-Terrestrial Physics*, 72(14), 1068–1079. <https://doi.org/10.1016/j.jastp.2010.07.002>
- Holton, J. R. (1982). The role of gravity wave induced drag and diffusion in the momentum budget of the mesosphere. *Journal of the Atmospheric Sciences*, 39(4), 791–799. [https://doi.org/10.1175/1520-0469\(1982\)039<0791:TROGWI>2.0.CO;2](https://doi.org/10.1175/1520-0469(1982)039<0791:TROGWI>2.0.CO;2)
- Huang, K. M., Liu, A. Z., Zhang, S. D., Yi, F., Huang, C. M., Gong, Y., et al. (2017). Simultaneous upward and downward propagating inertia-gravity waves in the MLT observed at Andes Lidar Observatory. *Journal of Geophysical Research: Atmospheres*, 122, 2812–2830. <https://doi.org/10.1002/2016JD026178>
- Huang, K. M., Liu, A. Z., Zhang, S. D., Yi, F., & Li, Z. (2012). Spectral energy transfer of atmospheric gravity waves through sum and difference nonlinear interactions. *Annales Geophysicae*, 30(2), 303–315. <https://doi.org/10.5194/angeo-30-303-2012>
- Huang, K. M., Yang, Z. X., Wang, R., Zhang, S. D., Huang, C. M., Yi, F., & Hu, F. (2018). A statistical study of inertia gravity waves in the lower stratosphere over the Arctic region based on radiosonde observations. *Journal of Geophysical Research: Atmospheres*, 123, 4958–4976. <https://doi.org/10.1029/2017JD027998>
- Huang, K. M., Zhang, S. D., & Yi, F. (2009). Gravity wave excitation through resonant interaction in a compressible atmosphere. *Geophysical Research Letters*, 36, L01803. <https://doi.org/10.1029/2008GL035575>
- Hu, X., Liu, A. Z., Gardner, C. S., & Swenson, G. R. (2002). Characteristics of quasi-monochromatic gravity waves observed with Na lidar in the mesopause region at Starfire Optical Range, NM. *Geophysical Research Letters*, 29(24), 2169. <https://doi.org/10.1029/2002GL014975>
- Krueger, D. A., She, C.-Y., & Yuan, T. (2015). Retrieving mesopause temperature and line-of-sight wind from full-diurnal-cycle Na lidar observations. *Applied Optics*, 54(32), 9469–9489. <https://doi.org/10.1364/AO.54.009469>
- Kuo, F.-S., Shen, H.-W., Fu, I.-J., Chao, J.-K., Röttger, J., & Liu, C.-H. (1985). Altitude dependence of vertical velocity spectra observed by VHF radar. *Radio Science*, 20(6), 1349–1354. <https://doi.org/10.1029/RS020i006p01349>
- Kwon, K. H., & Gardner, C. S. (1990). Airborne sodium lidar measurements of gravity wave intrinsic parameters. *Journal of Geophysical Research*, 95(D12), 20457–20467. <https://doi.org/10.1029/JD095iD12p20457>
- Larsen, M. F., Rutger, J., & Holden, D. N. (1987). Direct measurements of vertical-velocity power spectra with the SOUSY-VHF-Radar wind profiler system. *Journal of the Atmospheric Sciences*, 44(23), 3442–3448. [https://doi.org/10.1175/1520-0469\(1987\)044<3442:DMOV-VP>2.0.CO;2](https://doi.org/10.1175/1520-0469(1987)044<3442:DMOV-VP>2.0.CO;2)
- Larsen, M. F., Woodman, R. F., Sato, T., & Davis, M. K. (1986). Power spectra of oblique velocities in the troposphere and lower stratosphere observed at Arecibo, Puerto Rico. *Journal of the Atmospheric Sciences*, 43(20), 2230–2240. [https://doi.org/10.1175/1520-0469\(1986\)043<2230:PSOOVI>2.0.CO;2](https://doi.org/10.1175/1520-0469(1986)043<2230:PSOOVI>2.0.CO;2)
- Li, H. Y., Huang, C. M., Zhang, S. D., Huang, K. M., Zhang, Y., Gong, Y., et al. (2016). Low-frequency oscillations of the gravity wave energy density in the lower atmosphere at low latitudes revealed by U.S. radiosonde data. *Journal of Geophysical Research: Atmospheres*, 121, 13458–13473. <https://doi.org/10.1002/2016JD025435>
- Lindzen, R. S. (1981). Turbulence and stress owing to gravity wave and tidal breakdown. *Journal of Geophysical Research*, 86(C10), 9707–9714. <https://doi.org/10.1029/JC086iC10p09707>
- Li, Q., Rapp, M., Stober, G., & Latteck, R. (2018). High-resolution vertical velocities and their power spectrum observed with the MAARSY radar—Part 1: Frequency spectrum. *Annales Geophysicae*, 36(2), 577–586. <https://doi.org/10.5194/angeo-36-577-2018>
- Li, T., She, C. Y., Liu, H.-L., Leblanc, T., & McDermid, I. S. (2007). Sodium lidar-observed strong inertia-gravity wave activities in the mesopause region over Fort Collins, Colorado (41°N, 105°W). *Journal of Geophysical Research*, 112, D22104. <https://doi.org/10.1029/2007JD008681>
- Liu, A. Z., Guo, Y., Vargas, F., & Swenson, G. R. (2016). First measurement of horizontal wind and temperature in the lower thermosphere (105–140 km) with a Na Lidar at Andes Lidar Observatory. *Geophysical Research Letters*, 43, 2374–2380. <https://doi.org/10.1002/2016GL068461>
- Liu, H.-L., & Meriwether, J. W. (2004). Analysis of a temperature inversion event in the lower mesosphere. *Journal of Geophysical Research*, 109, D02S07. <https://doi.org/10.1029/2002JD003026>
- Lu, X., Chen, C., Huang, W., Smith, J. A., Chu, X., Yuan, T., et al. (2015). A coordinated study of 1 h mesoscale gravity waves propagating from Logan to Boulder with CRRL Na Doppler lidars and temperature mapper. *Journal of Geophysical Research: Atmospheres*, 120, 10006–10021. <https://doi.org/10.1002/2015JD023604>
- Lu, X., Chu, X., Li, H., Chen, C., Smith, J. A., & Vadas, S. L. (2017). Statistical characterization of high-to-medium frequency mesoscale gravity waves by lidar-measured vertical winds and temperatures in the MLT. *Journal of Atmospheric and Solar-Terrestrial Physics*, 162, 3–15. <https://doi.org/10.1016/j.jastp.2016.10.009>
- Moffat-Griffin, T., Hibbins, R. E., Jarvis, M. J., & Colwell, S. R. (2011). Seasonal variations of gravity wave activity in the lower stratosphere over an Antarctic Peninsula station. *Journal of Geophysical Research*, 116, D14111. <https://doi.org/10.1029/2010JD015349>
- Muschinski, A., Chilson, P. B., Hooper, D. A., Palmer, R. D., Schmidt, G., & Steinhagen, H. (2001). Boundary-layer convection and diurnal variation of vertical-velocity characteristics in the free troposphere. *Quarterly Journal of the Royal Meteorological Society*, 127(572), 423–443. <https://doi.org/10.1002/qj.49712757210>
- Nastrom, G. D., & Eaton, F. D. (2006). Quasi-monochromatic inertia-gravity waves in the lower stratosphere from MST radar observations. *Journal of Geophysical Research*, 111, D19103. <https://doi.org/10.1029/2006JD007335>
- Nicolls, M. J., Varney, R. H., Vadas, S. L., Stamus, P. A., Heinselman, C. J., Cosgrove, R. B., & Kelley, M. C. (2010). Influence of an inertia-gravity wave on mesospheric dynamics: A case study with the Poker Flat Incoherent Scatter Radar. *Journal of Geophysical Research*, 115, D00N02. <https://doi.org/10.1029/2010JD014042>
- Plougonven, R., Teitelbaum, H., & Zeitlin, V. (2003). Inertia gravity wave generation by the tropospheric midlatitude jet as given by the Fronts and Atlantic Storm-Track Experiment radio soundings. *Journal of Geophysical Research*, 108(D21), 4686. <https://doi.org/10.1029/2003JD003535>

- Qing, H., Zhou, C., Zhao, Z., Chen, G., Ni, B., Gu, X., et al. (2014). A statistical study of inertia gravity waves in the troposphere based on the measurements of Wuhan Atmosphere Radio Exploration (WARE) radar. *Journal of Geophysical Research: Atmospheres*, 119, 3701–3714. <https://doi.org/10.1002/2013JD020684>
- Rajeev, K., Parameswaran, K., Sasi, M. N., Ramkumar, G., & Krishna Murthy, B. V. (2003). Rayleigh lidar observations of quasi-sinusoidal waves in the tropical middle atmosphere. *Journal of Geophysical Research*, 108(D24), 4749. <https://doi.org/10.1029/2003JD003682>
- Ratnam, M. V., Babu, A. N., Rao, V. V. M. J., Rao, S. V. B., & Rao, D. N. (2008). MST radar and radiosonde observations of inertia-gravity wave climatology over tropical stations: Source mechanisms. *Journal of Geophysical Research*, 113, D07109. <https://doi.org/10.1029/2007JD008986>
- Scargle, J. D. (1982). Studies in astronomical time series analysis. II—Statistical aspects of spectral analysis of unevenly spaced data. *The Astrophysical Journal*, 263.
- Senft, D. C., & Gardner, C. S. (1991). Seasonal variability of gravity wave activity and spectra in the mesopause region at Urbana. *Journal of Geophysical Research*, 96(D9), 17229–17264. <https://doi.org/10.1029/91JD01662>
- She, C. Y., & Yu, J. R. (1994). Simultaneous three-frequency Na lidar measurements of radial wind and temperature in the mesopause region. *Geophysical Research Letters*, 21(17), 1771–1774. <https://doi.org/10.1029/94GL01417>
- Smith, S. A., Fritts, D. C., & Vanzandt, T. E. (1987). Evidence for a saturated spectrum of atmospheric gravity waves. *Journal of the Atmospheric Sciences*, 44(10), 1404–1410. [https://doi.org/10.1175/1520-0469\(1987\)044<1404:EFASSO>2.0.CO;2](https://doi.org/10.1175/1520-0469(1987)044<1404:EFASSO>2.0.CO;2)
- Snively, J. B. (2017). Nonlinear gravity wave forcing as a source of acoustic waves in the mesosphere, thermosphere, and ionosphere. *Geophysical Research Letters*, 44, 12020–12027. <https://doi.org/10.1002/2017GL075360>
- Suzuki, H., Nakamura, T., Vadas, S. L., Tsutsumi, M., Taguchi, M., & Fujiwara, Y. (2013). Inertia-gravity wave in the polar mesopause region inferred from successive images of a meteor train. *Journal of Geophysical Research: Atmospheres*, 118, 3047–3052. <https://doi.org/10.1002/jgrd.50228>
- Tsuda, T., Murayama, Y., Wiryosumarto, H., Harijono, S. W. B., & Kato, S. (1994). Radiosonde observations of equatorial atmosphere dynamics over Indonesia: 1. Equatorial waves and diurnal tides. *Journal of Geophysical Research*, 99(D5), 10491–10505. <https://doi.org/10.1029/94JD00355>
- VanZandt, T. E. (1982). A universal spectrum of buoyancy waves in the atmosphere. *Geophysical Research Letters*, 9(5), 575–578. <https://doi.org/10.1029/GL009i005p00575>
- Vincent, R. A., & Alexander, M. J. (2000). Gravity waves in the tropical lower stratosphere: An observational study of seasonal and interannual variability. *Journal of Geophysical Research*, 105(D14), 17971–17982. <https://doi.org/10.1029/2000JD900196>
- Wang, L., Geller, M. A., & Alexander, M. J. (2005). Spatial and temporal variations of gravity wave parameters. Part I: Intrinsic frequency, wavelength, and vertical propagation direction. *Journal of the Atmospheric Sciences*, 62, 125–142. <https://doi.org/10.1175/JAS-3364.1>
- Weinstock, J. (1989). Saturated and unsaturated spectra of gravity waves and scale-dependent diffusion. *Journal of the Atmospheric Sciences*, 47(18), 2211–2226. [https://doi.org/10.1175/1520-0469\(1990\)047<2211:SAUSOG>2.0.CO;2](https://doi.org/10.1175/1520-0469(1990)047<2211:SAUSOG>2.0.CO;2)
- Wu, Y., Xu, J., Yuan, W., Chen, H., & Bian, J. (2006). Spectral analysis of 10-m resolution temperature profiles from balloon soundings over Beijing. *Annales Geophysicae*, 24(7), 1801–1808. <https://doi.org/10.5194/angeo-24-1801-2006>
- Xu, J., Smith, A. K., Collins, R. L., & She, C.-Y. (2006). Signature of an overturning gravity wave in the mesospheric sodium layer: Comparison of a nonlinear photochemical-dynamical model and lidar observations. *Journal of Geophysical Research*, 111, D17301. <https://doi.org/10.1029/2005JD006749>
- Yamamori, M., & Sato, K. (2006). Characteristics of inertia gravity waves over the South Pacific as revealed by radiosonde observations. *Journal of Geophysical Research*, 111, D16110. <https://doi.org/10.1029/2005JD006861>
- Yamamoto, M., Tsuda, T., Kato, S., Sato, T., & Fukao, S. (1987). A saturated inertia gravity wave in the mesosphere observed by the middle and upper atmosphere radar. *Journal of Geophysical Research*, 92(D10), 11993–11999. <https://doi.org/10.1029/JD092iD10p11993>
- Yamamoto, Y., Tsuda, T., & Adachi, T. (1996). Frequency spectra of wind velocity and temperature fluctuations observed with the MU radar-RASS. *Geophysical Research Letters*, 23(24), 3647–3650. <https://doi.org/10.1029/96GL03374>
- Yang, G., Clemesha, B., Batista, P., & Simonich, D. (2006). Gravity wave parameters and their seasonal variations derived from Na lidar observations at 23°S. *Journal of Geophysical Research*, 111, D21107. <https://doi.org/10.1029/2005JD006900>
- Yang, G., Clemesha, B., Batista, P., & Simonich, D. (2010). Seasonal variations of gravity wave activity and spectra derived from sodium temperature lidar. *Journal of Geophysical Research*, 115, D18104. <https://doi.org/10.1029/2009JD012367>
- Yoshiki, M., Kizu, N., & Sato, K. (2004). Energy enhancements of gravity waves in the Antarctic lower stratosphere associated with variations in the polar vortex and tropospheric disturbances. *Journal of Geophysical Research*, 109, D23104. <https://doi.org/10.1029/2004JD004870>
- Yuan, T., Heale, C. J., Snively, J. B., Cai, X., Pautet, P.-D., Fish, C., et al. (2016). Evidence of dispersion and refraction of a spectrally broad gravity wave packet in the mesopause region observed by the Na lidar and Mesospheric Temperature Mapper above Logan, Utah. *Journal of Geophysical Research: Atmospheres*, 121, 579–594. <https://doi.org/10.1002/2015JD023685>
- Yuan, T., Pautet, P.-D., Zhao, Y., Cai, X., Criddle, N. R., Taylor, M. J., & Pendleton, W. R., Jr. (2014). Coordinated investigation of midlatitude upper mesospheric temperature inversion layers and the associated gravity wave forcing by Na lidar and Advanced Mesospheric Temperature Mapper in Logan, Utah. *Journal of Geophysical Research: Atmospheres*, 119, 3756–3769. <https://doi.org/10.1002/2013JD020586>
- Zhang, F., Wang, S., & Plougonven, R. (2004). Uncertainties in using the hodograph method to retrieve gravity wave characteristics from individual soundings. *Geophysical Research Letters*, 31, L11110. <https://doi.org/10.1029/2004GL019841>
- Zhang, S. D., Huang, C. M., Huang, K. M., Gong, Y., Chen, G., Gan, Q., & Zhang, Y. H. (2017). Latitudinal and seasonal variations of vertical wave number spectra of three-dimensional winds revealed by radiosonde observations. *Journal of Geophysical Research: Atmospheres*, 122, 13174–13190. <https://doi.org/10.1002/2017JD027602>
- Zhang, S. D., & Yi, F. (2005). A statistical study of gravity waves from radiosonde observations at Wuhan (30°N, 114°E) China. *Annales Geophysicae*, 23(3), 665–673. <https://doi.org/10.5194/angeo-23-665-2005>
- Zhang, S. D., & Yi, F. (2007). Latitudinal and seasonal variations of inertial gravity wave activity in the lower atmosphere over central China. *Journal of Geophysical Research*, 112, D05109. <https://doi.org/10.1029/2006JD007487>
- Zhang, S. D., Yi, F., Huang, C. M., & Huang, K. M. (2012). High vertical resolution analyses of gravity waves and turbulence at a midlatitude station. *Journal of Geophysical Research*, 117, D02103. <https://doi.org/10.1029/2011JD016587>
- Zhang, S. D., Yi, F., Huang, C. M., Huang, K. M., Gan, Q., Zhang, Y. H., & Gong, Y. (2013). Latitudinal and altitudinal variability of lower atmospheric inertial gravity waves revealed by U.S. radiosonde data. *Journal of Geophysical Research: Atmospheres*, 118, 7750–7764. <https://doi.org/10.1002/jgrd.50623>
- Zhou, Q., & Morton, Y. T. (2006). A case study of mesospheric gravity wave momentum flux and dynamical instability using the Arecibo dual beam incoherent scatter radar. *Geophysical Research Letters*, 33, L18082. <https://doi.org/10.1029/2005GL025608>

- Zhu, X. (1994). A new theory of the saturated gravity wave spectrum for the middle atmosphere. *Journal of the Atmospheric Sciences*, 51(24), 3615–3626. [https://doi.org/10.1175/1520-0469\(1994\)051<3615:ANTOTS>2.0.CO;2](https://doi.org/10.1175/1520-0469(1994)051<3615:ANTOTS>2.0.CO;2)
- Zink, F., & Vincent, R. A. (2001). Wavelet analysis of stratospheric gravity wave packets over Macquarie Island: 1. Wave parameters. *Journal of Geophysical Research*, 106(D10), 10275–10288. <https://doi.org/10.1029/2000JD900847>